Proceedings of The 2018 IEEE International
Conference on Real-time Computing and Robotics
August 1-5, 2018, Kandima, Maldives

Dynamic Modeling and Characterization of the Core-XY Cartesian Motion System

Mingzhou Yin*, Yue Chen*, Kit-Hang Lee, Denny K.C. Fu, Zion Tsz Ho Tse, Ka-Wai Kwok, *Member, IEEE*

***Abstract*— Cartesian motion systems have been key in the development of precise positioning machines with micro-scale accuracy for various applications. Technologies such as 3D printers, laser cutters, and automated tissue indentation platforms utilize Cartesian motion systems for improved accuracy. A promising parallel belt-driven mechanism called Core-XY has been proposed to reduce the moving load of the system. It has been demonstrated that Core-XY outperforms conventional Cartesian motion systems, where motion in each dimension is actuated by a separate motor. However, the elasticity of the belt transmission inevitably induces unneglectable errors under high running speed while moving along a defined trajectory. This project's objective is to thoroughly identify the sources of such errors by dynamic modeling of the Core-XY Cartesian motion system. Detailed dynamic modeling methods with both full degrees of freedom (DoFs) and simplified DoFs are presented. Error analysis of the Core-XY system was conducted based on the dynamic model, along with experimental validation, under different operation conditions. The proposed dynamic model attained accurate estimation of contour errors, which is important to the design of the motion controller for systems adopting Core-XY mechanism.**

***Index Terms*— Core-XY system, Cartesian motion system, dynamic modeling, belt transmission**

I. Introduction

THE Cartesian motion system, namely XY-table, is a device capable of positioning the end-effector at desired coordinates within a two-dimensional plane. This device is adopted in many Computer Numeric Controlled (CNC) manufacturing processes, including milling, cutting, welding, and marking [1-3]. In addition, majority of 3D printers utilize this mechanism to achieve the in-plane actuation [4].

Various designs and implementations of the Cartesian motion systems have been proposed, which are mainly categorized by the transmission approaches that transform rotational motion to translational motion. The transmissions are either the lead-screw-based form [5, 6] or belt-driven [3]. The well-known lead-screw-based system consists of two separate orthogonal linear actuators with lead screws, one mounted on the top of the other. Due to its rigidity, the lead-screw-based mechanism is advantageous to enable high-resolution and large-payload actuation for precision positioning applications, such as CNC milling machines. However, the disadvantages are attributed to its large moving mass. Because of this, the running speed is typically slow. In contrast, not only does the belt-driven mechanism consume less energy (around 50~70% less), but it can also operate at relatively fast speeds, 2-10 times faster [7] than the lead-screw-based systems. Moreover, the manufacturing cost of the belt-driven mechanism is rather low, due to its design simplicity. Recent applications in 3D printing incorporate the belt-driven mechanism combined with a vertical linear actuator to provide the 3D spatial motion of the printer nozzle. The motion accuracy heavily relies on the stiffness of the belts.

Other than transmission methods, the Cartesian motion system can also be categorized into serial and parallel manipulations, such that two independent actuations can be linked, either in series or parallel. The serial manipulation, despite being widely used, has significant disadvantages caused by its low load/weight ratio and sensitivity to error [8]. In the scenario of the Cartesian motion systems, one of the actuators acts as a sub-system implemented on the other actuator where an unnecessary load is added. The two axes of motion are inherently decoupled. Motion control can only be applied on one separated dimension/direction, rather than the 2D position. Therefore, the serial manipulation can neither regulate contour errors directly nor satisfy applications at high speed with low-power consumption. In comparison, the parallel manipulation can coordinate the motion at a faster speed with higher power efficiency. Such a light-weight mechanism could also be compactly integrated. This is preferable for low-payload applications such as desktop 3D printing.

The H-frame system [9] is a promising parallel mechanism operated with one single belt. It has two motors which are located at fixed positions (**Fig. 1**). However, because the end-effector is connected to two flexible ends of the belt, it is unstable. To correct this instability, a modified version of the H-frame system has been developed, namely the Core-XY system [10]. The Core-XY allows motor integration with a different configuration of the two belts. As shown in **Fig. 1**,

**This work is supported in parts by the Croucher Foundation and the Research Grants Council (RGC) of Hong Kong (Ref. No. 27209515, No. 17227616, and No. 17202317).

Mingzhou Yin, Kit-Hang Lee, Denny K.C. Fu, and Ka-Wai Kwok, are with the Department of Mechanical Engineering, The University of Hong Kong, Hong Kong, China.

Yue Chen was with the Department of Mechanical Engineering, The University of Hong Kong, Hong Kong, China and he is now with the Department of Mechanical Engineering, Vanderbilt University, Nashville, TN, USA, 37212.

Zion Tsz Ho Tse is with the College of Engineering, The University of Georgia, Athens, GA, USA, 30602.

*indicates Co-first author. Corresponding author: Ka-Wai Kwok, email: kwokkw@hku.hk

978-1-5386-6869-6/18/$31.00 ©

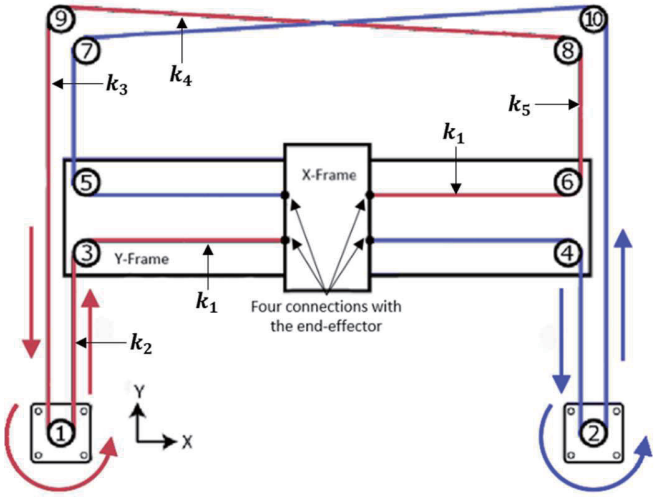

Fig. 1. Schematics of Core-XY system, two belts (in red and blue) connected with the end-effector at four points symmetrically. Components 1 and 2 are the stationary driving units in both sub-figures; Components 3-10 are the idle pulleys.

four ends of the belt link with the end-effector symmetrically, thus ensuring motion stability. A detailed comparison between these two mechanisms is discussed in *Section II*.

However, the unneglectable stiffness of the belt, which makes itself deformable, does degrade the overall positioning accuracy of the Core-XY system. To tackle this problem, several control methods have been applied to conventional serial positioning systems. This includes adaptive control [11-13], inertial and friction compensation [7], fuzzy logic [14], and sliding mode control (SMC) methods [15, 16]. In positioning control of two-dimensional Cartesian motion systems, Lim *et al* [1] emphasized the error induced by the stiffness of elastic transmission elements; Li *et al* pointed out the significance of the inertia and the friction in a one-dimensional belt-driven positioning system [7]. Therefore, proper identification of system dynamics is essential, as well as its modeling. To the best of our survey, none of the work conducted was done on the dynamic modelling of the Core-XY system or the contour error analysis of any parallel Cartesian motion systems, despite such systems showing significant contour errors due to their dynamic nature.

II. Materials and Methods

This section starts by discussing the characteristics of the Core-XY mechanism. Kinematics modeling is proposed for the targeting of this mechanism. Furthermore, in order to predict the actual positioning in real time, dynamic modeling is derived, considering practical design parameters including inertia, stiffness, and friction.

A. The Core-XY Mechanism

The Core-XY system consists of ten timing pulleys (two driving pulleys and eight idle pulleys), two open-ended timing belts, a *y*-frame to anchor four idle pulleys in motion, and the *x*-frame acting as end-effector (**Fig. 1**). By rotating both motors in the same direction at the same speed, the end-effector moves in the x-direction only, whereas by rotating in the opposite direction at the same speed, the end-effector moves in the y-direction only. Detailed equations are discussed in the Section II.B.

B. Kinematics Modeling

If belts are assumed inextensible, the position of the end-effector can be determined directly from the angular displacements of the motors. The kinematic relations between the rotating angles of driving pulleys 1, 2 $(\Delta\varphi_1\ \Delta\varphi_2)^T$ and the position of the end-effector $(\Delta x\ \Delta y)^T$ are given by:

$$\begin{pmatrix}\Delta x\\ \Delta y\end{pmatrix}=\frac{r}{2}\begin{bmatrix}1 & 1\\ 1 & -1\end{bmatrix}\begin{pmatrix}\Delta\varphi_1\\ \Delta\varphi_2\end{pmatrix} \tag{1}$$

where r is the radius of the pulley.

The defect of (1) lies in the inextensible assumption. Under this assumption, the motion is transmitted instantaneously with infinite acceleration by infinitely large force, which fails to stress the effect of stiffness, inertia, and friction inside the system. As a result, the transient performance of the system cannot be illustrated. Therefore, the dynamic modeling taking the above factors into account is derived using Lagrange's equations of the second kind as follows:

$$\frac{\partial}{\partial t}\left(\frac{\partial L}{\partial \dot{q}_i}\right)-\frac{\partial L}{\partial q_i}=Q_i^{nc},\ L=T-V \tag{2}$$

where q_i is the i^{th} generalized coordinate; Q_i^{nc} is the non-conservative generalized forces on the i^{th} generalized coordinate; T is the total kinetic energy of the system; V is the total potential energy of the system.

C. Dynamic Modeling

The system is modeled with 12 DoFs with generalized coordinates chosen as follows:

$$\mathbf{q}=\begin{pmatrix}x & y & \varphi_1 & \varphi_2 & \dots & \varphi_{10}\end{pmatrix}^T \tag{3}$$

where x and y define the position of the end-effector; φ_i is the rotating angle of the i^{th} pulley in **Fig. 1**. The belts are regarded as a 'spring with mass' system [17]. The kinetic energy, potential energy, and virtual work done by non-conservative forces are given in the following so as to construct the dynamic model using Lagrange's equation of motion.

1) Kinetic Energy

The total kinetic energy is given by:

$$T=\frac{1}{2}m_x\dot{x}^2+\frac{1}{2}M\dot{y}^2+\frac{1}{2}\sum_i^{10}J_{p,i}\dot{\varphi}_i^2 \tag{4}$$

where m_x is the equivalent mass of the end-effector; $M=m_y+m_1+m_{p,3}+m_{p,4}+m_{p,5}+m_{p,6}$ is the equivalent mass of the *y*-frame; m_y is the mass of the *y*-frame; $m_{p,i}$ is the equivalent mass of the i^{th} pulley; $J_{p,i}$ is the equivalent moment of inertia of the i^{th} pulley.

The equivalent masses (moments of inertia) in the above equations include the masses of the adjacent belt sections. The kinetic energy stored in the belt can be denoted:

$$T_{belt}=\int_0^l\frac{1}{2}\left(v_1+\frac{v_2-v_1}{l}x\right)^2\rho A dx=\frac{1}{2}m_{belt}\frac{v_1^2+v_1v_2+v_2^2}{3} \tag{5}$$

where l is the length of the belt; v_1, v_2 are velocities at two ends; ρ is the density of the belt; A is the cross-section area of

the belt; m_{belt} is the mass of belt. In Cartesian motion systems, stiffness of belts is typically very high to attain a high accuracy, i.e. $v_1 \approx v_2$. Therefore, masses of belts can be averaged to adjacent coordinates within a reasonable error range.

2) Elastic Potential Energy

When located horizontally, the potential energy in the system is the elastic energy stored in the belts, which is given by:

$$\begin{aligned} V = &\frac{1}{2}k_1\left[\left(r\varphi_3 + x\right)^2 + \left(r\varphi_4 + x\right)^2 + \left(r\varphi_6 - x\right)^2 + \left(r\varphi_5 - x\right)^2\right] \\ &+\frac{1}{2}k_2\left[\left(r\varphi_3 + r\varphi_1 - y\right)^2 + \left(r\varphi_4 + r\varphi_2 + y\right)^2\right] \\ &+\frac{1}{2}k_3\left[\left(r\varphi_9 - r\varphi_1\right)^2 + \left(r\varphi_{10} - r\varphi_2\right)^2\right] \\ &+\frac{1}{2}k_4\left[\left(r\varphi_9 - r\varphi_8\right)^2 + \left(r\varphi_{10} - r\varphi_7\right)^2\right] \\ &+\frac{1}{2}k_5\left[\left(r\varphi_8 - r\varphi_6 - y\right)^2 + \left(r\varphi_7 - r\varphi_5 + y\right)^2\right] \end{aligned} \tag{6}$$

where k_i is the stiffness of the i^{th} belt section as defined in **Fig. 1**. The same k-value is assumed for the symmetrical belt sections.

Equation (6) is derived when there is no slipping between pulleys and belts. This condition could be guaranteed using timing pulleys and belts, as in our experiment setup.

3) Virtual Work of Non-Conservative Forces

For DC-motor-driven systems, both friction and torques exerted by motors are regarded as non-conservative forces. The virtual work done by non-conservative forces could be expressed as:

$$\begin{aligned} \delta W^{nc} &= -\left[b_1\dot{x} + f_1 sgn\left(\dot{x}\right)\right]\delta x - \left[b_2\dot{y} + f_2 sgn\left(\dot{y}\right)\right]\delta y \\ &\quad -\sum_i^{10}\left[B_p\dot{\varphi}_i + \tau_f sgn\left(\dot{\varphi}_i\right)\right]\delta\varphi_i + \tau_1\delta\varphi_1 + \tau_2\delta\varphi_2 \\ &= \sum_i Q_i^{nc}\delta q_i \end{aligned} \tag{7}$$

where b_1, b_2 are viscous friction coefficients of the end-effector and the y-frame respectively; f_1, f_2 are the Coulomb friction of the end-effector and the y-frame respectively; B_p is the viscous friction coefficient of one pulley; τ_f is the Coulomb friction torque of one pulley; $\tau_i = K_1 V_i - K_2\dot{\varphi}_i$ is the torque exerted by the i^{th} motor, where V_i is the input voltage to the i^{th} motor.

In the case of motion driven by stepper motors, with the angles of driving pulleys φ_1 and φ_2 directly regarded as input, only friction is considered as a non-conservative force.

The aforementioned parameters are assembled into (2). For the motion driven by stepper motors, the dynamics could be modeled as:

$$\ddot{x} = \frac{1}{m_1}\left[-b_1\dot{x} - 4k_1 x + rk_1\left(\varphi_5 + \varphi_6 - \varphi_3 - \varphi_4\right) - f_1 sgn\left(\dot{x}\right)\right]$$

$$\begin{aligned} \ddot{y} = \frac{1}{M}\Big[&-b_2\dot{y} - 2\left(k_2 + k_5\right)y + rk_2\left(\varphi_1 + \varphi_3 - \varphi_2 - \varphi_4\right) \\ &+rk_5\left(\varphi_5 + \varphi_8 - \varphi_6 - \varphi_7\right) - f_2 sgn\left(\dot{y}\right)\Big] \end{aligned}$$

$$\ddot{\varphi}_i = \begin{cases} \dfrac{1}{J_{p,i}}\begin{bmatrix} -B_p\dot{\varphi}_i - \left(k_m + k_n\right)r^2\varphi_i - rk_m x \\ +rk_n y - r^2 k_m\varphi_s - \tau_f sgn\left(\dot{\varphi}_i\right) \end{bmatrix}, & i = 3,4,5,6 \\ \dfrac{1}{J_{p,i}}\begin{bmatrix} -B_p\dot{\varphi}_i - \left(k_m + k_n\right)r^2\varphi_i - rk_n y \\ +r^2\left(k_n\varphi_s - k_m\varphi_t\right) - \tau_f sgn\left(\dot{\varphi}_i\right) \end{bmatrix}, & i = 7,8,9,10 \end{cases}$$

$$\text{where}\begin{cases} m = 1, n = 2, s = i-2; & \text{for } i = 3,4 \\ m = 5, n = 1, s = i+2; & \text{for } i = 5,6 \\ m = 4, n = 5, s = 15-t, t = i-2; & \text{for } i = 7,8 \\ m = 3, n = 4, s = i-8, t = 9-s; & \text{for } i = 9,10 \end{cases} \tag{8}$$

The state-space representations are designed as follows:

$$\begin{cases} \boldsymbol{\chi}(\mathbf{t}) = \begin{pmatrix} x & \dot{x} & y & \dot{y} & \varphi_3 & \dot{\varphi}_3 & \cdots & \varphi_{10} & \dot{\varphi}_{10} \end{pmatrix}^T \\ \mathbf{u}(\mathbf{t}) = \begin{pmatrix} \varphi_1 & \varphi_2 \end{pmatrix}^T \\ \boldsymbol{\psi}(\mathbf{t}) = \begin{pmatrix} x & y \end{pmatrix}^T \end{cases} \tag{9}$$

where $\boldsymbol{\chi}(\mathbf{t})$ is the state vector; $\mathbf{u}(\mathbf{t})$ is the input vector; $\boldsymbol{\psi}(\mathbf{t})$ is the output vector.

For the motion driven by DC motors, additional equations are needed to describe the motor dynamics of φ_1 and φ_2 with $(x \quad \dot{x} \quad y \quad \dot{y} \quad \varphi_1 \quad \dot{\varphi}_1 \quad \ldots \quad \varphi_{10} \quad \dot{\varphi}_{10})^T$ as state vector and $(V_1 \quad V_2)^T$ as input:

$$\ddot{\varphi}_i = \frac{1}{J_{p,i}}\begin{bmatrix} -\left(B_p + K_2\right)\dot{\varphi}_i - \left(k_2 + k_3\right)r^2\varphi_i \\ +rk_2 y + r^2\left(k_3\varphi_{i+8} - k_2\varphi_{i+2}\right) \\ +K_1 V_i - \tau_f sgn\left(\dot{\varphi}_i\right) \end{bmatrix}, i = 1,2. \tag{10}$$

D. Simplified 4-DoF Dynamic Modeling

The movement of idle pulleys is regarded as less insignificant than that of driving pulleys and the end-effector in [9]. The number of DoF in the dynamic modeling can be reduced by assigning the DoFs of idle pulleys to other DoFs. In detail, pulley 3, 4, 5 and 6 are only related to x-direction motion whereas pulley 7, 8, 9 and 10 are related to both x- and y-direction motion. Therefore, pulley 3, 4, 5 and 6 can be assigned to the coordinate x; pulley 8 and 9 can be assigned to the coordinate φ_1; pulley 7 and 10 can be assigned to the coordinate φ_2.

Similar simplified modeling could be carried out by revising the definitions of generalized coordinates, kinetic energy, potential energy, and virtual work done by non-conservative forces, as follows:

$$\mathbf{q} = \begin{pmatrix} x & y & \varphi_1 & \varphi_2 \end{pmatrix}^T \tag{11}$$

$$T = \frac{1}{2}m_{xe}\dot{x}^2 + \frac{1}{2}M\dot{y}^2 + \frac{1}{2}J_{1e}\dot{\varphi}_1^2 + \frac{1}{2}J_{2e}\dot{\varphi}_2^2 \tag{12}$$

where $m_{xe} = m_x + \frac{J_{p,3}+J_{p,4}+J_{p,5}+J_{p,6}}{r^2}$, $J_{1e} = J_{p,1} + J_{p,7} + J_{p,10}$, $J_{2e} = J_{p,2} + J_{p,8} + J_{p,9}$

$$V = \frac{1}{2}k_e\left[\left(r\varphi_1 - x - y\right)^2 + \left(r\varphi_2 - x + y\right)^2\right] \tag{13}$$

where $k_e = \frac{k_1 k_2}{k_1 + k_2} + \frac{k_1 k_3 k_4 k_5}{k_1 k_3 k_4 + k_1 k_3 k_5 + k_1 k_4 k_5 + k_3 k_4 k_5}$

$$\begin{aligned}\delta W^{nc} &= -\left[b_{1e}\dot{x} + f_{1e}sgn(\dot{x})\right]\delta x - \left[b_2\dot{y} + f_2 sgn(\dot{y})\right]\delta y \\ &+\left[\tau_1 - B_{pe}\dot{\varphi}_i - \tau_{fe}sgn(\dot{\varphi}_i)\right]\delta\varphi_1 \\ &+\left[\tau_2 - B_{pe}\dot{\varphi}_i - \tau_{fe}sgn(\dot{\varphi}_i)\right]\delta\varphi_2 \\ &= \sum_i Q_i^{nc}\delta q_i\end{aligned} \quad (14)$$

where $b_{1e} = b_1 + 4\frac{B_p}{r^2}$, $f_{1e} = f_1 + 4\frac{B_p}{r}$, $B_{pe} = 3B_p$, $\tau_{fe} = 3\tau_f$

For stepper-motor-driven systems, the final modeling results are given by

$$\begin{aligned}\ddot{x} &= \frac{1}{m_{1e}}\left[-b_{1e}\dot{x} - 2k_e x + rk_e(\varphi_1 + \varphi_2) - f_{1e}\,\mathrm{sgn}(\dot{x})\right] \\ \ddot{y} &= \frac{1}{M}\left[-b_2\dot{y} - 2k_e y + rk_e(\varphi_1 - \varphi_2) - f_2\,\mathrm{sgn}(\dot{y})\right]\end{aligned} \quad (15)$$

with the state vector involving *x* and *y* only.

For DC-motor-driven systems, the equations of φ_1 and φ_2 are:

$$\ddot{\varphi}_i = \frac{1}{J_{p,ie}}\begin{bmatrix}-\left(B_{pe} + K_2\right)\dot{\varphi}_i - k_e r^2\varphi_i + rk_e\left(x + my\right) \\ +K_1 V_i - \tau_{fe}\,\mathrm{sgn}\left(\dot{\varphi}_i\right)\end{bmatrix}, i = 1,2 \quad (16)$$

where $m = 1$ for $i = 1$, $m = -1$ for $i = 2$ with the state vector involving *x*, *y*, φ_1, and φ_2.

However, the validity of these simplifications remains to be proved. The discrepancy between the full-DoF model and the 4-DoF model is illustrated by simulations and experimental validations in *Section III*.

III. Simulation and Experimental Results

To experimentally compare the full-DoF and the 4-DoF dynamic models with the kinematic model, the experimental results were used as a baseline to highlight the contour errors in tasks of a rectangular path. Then, the effect of different mechanical setups on the magnitude of the contour error was discussed.

Cartesian motion systems are often realized with open-loop stepper-motor-driven configuration for simple and low-cost applications. The tradeoff arises between accuracy and manufacturing cost. This type of configuration is adopted in both simulations and experiments to evaluate the accuracy of the dynamic modeling as well as the performance of the Core-XY system.

Fig. 2 shows the experiment setup. The baseplate and the *y*-frame were made of acrylic board by laser cutting whereas the rigid end-effector was 3D-printed with four belt clips to anchor the belts. To ensure safe anchoring with belt clips, the belts connected to the end-effector are not strictly horizontal. However, the linear guides made of carbon fiber can guarantee perfect Cartesian motion of the end-effector. MXL timing pulleys were connected to the baseplate with shoulder screws. Two stepper motors with a phase angle resolution of 1.8° were chosen, of which the driver board TB6560 was used. Open-loop control was realized by the open-source electronics platform Arduino. Positional tracking of the given experimental trajectory was conducted by an electromagnetic tracking system (NDI Aurora). Stiffness of the belt is calculated by

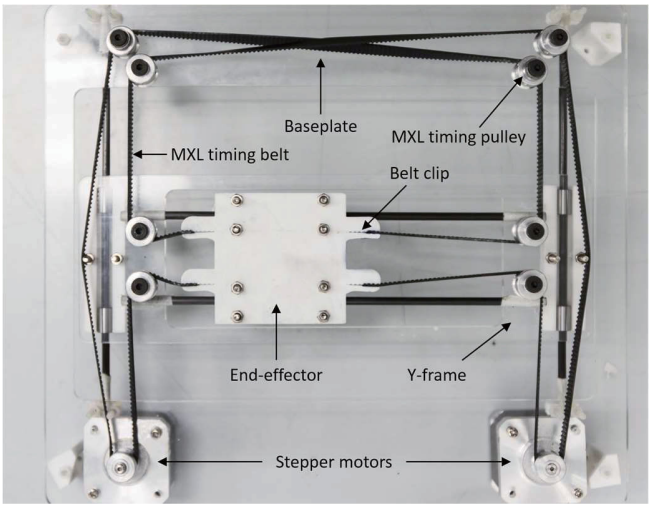

Fig. 2. Experiment setup of a Core-XY mechanism actuated by NEMA-17 stepper motor through two MXL timing belts.

elastic theory $k = (A \cdot E)/l$, where A is the cross-section area of the belt, l is length of the belt section, E is young's modulus of the belt (for the MXL timing belt adopted, $E = 160MPa$).

A. Trajectory Tracking Analysis

Study of the transient behaviour is pre-requisite to reducing overall system error. This would explain why the end-point targeting accuracy always outperforms the ones in contour tracking in real practices. In both simulated and experimental results, when the end-effector moved along a smooth contour (e.g., line or circle), no obvious error was observed. Under normal operating conditions, the settling time of the system was typically very small.

As observed, the end-effector does not always move accurately and smoothly along the contour at the sharp turning curvature. In this case, there is always a time lag from executing the actual position of the end-effector to the ideal position because of the control undershoot. The end-effector turns before reaching the corner point. As a result, the actual trajectory will be rounded at the sharp corner. To investigate this phenomenon, tasks of rectangular path following at different running speeds were carried out through simulations and experiments. The resulting trajectories of the full-DoF simulation, the 4-DoF simulation and the real robot experiments, are shown in **Fig. 3a, b** and **c**, with respect to different running speeds.

Nearly no deviations from the ideal trajectory were observed while moving along a straight line (**Fig. 3**). Larger error was found in both the experiments and simulations while turning from *x*- to *y*-direction, compared to the turning from *y*- to *x*-direction. The *x*-direction had a larger settling time than the *y*-direction. It led to a longer lag when the signal of turning was executed, thus inducing larger error, particularly at a higher running speed that leaves less time for the end-effector to settle its position. Therefore, it can be presumed that if the time interval per pulse is longer than the settling time, no contour error that resulted from the system dynamics will be observed within the 5% range as defined for the settling time.

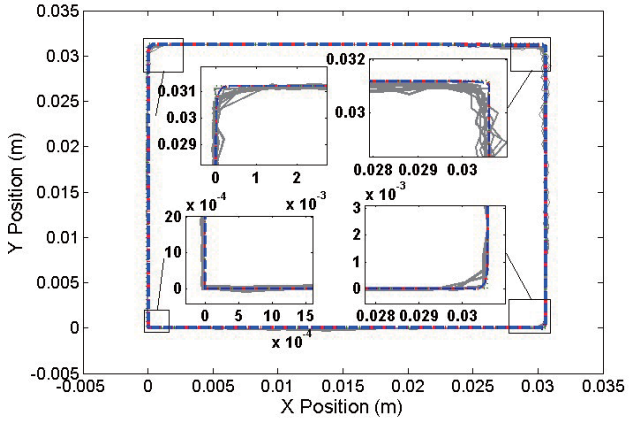

(a)

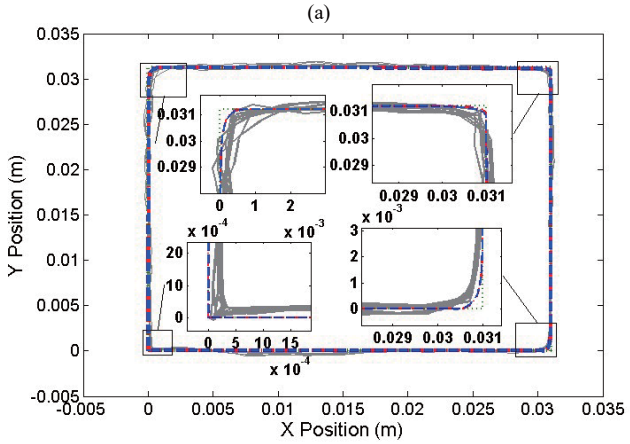

(b)

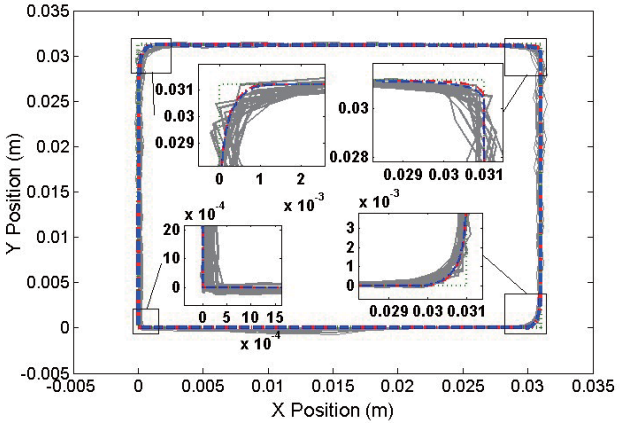

(c)

Fig. 3. Trajectory comparison of experiment and simulation under running speed of (a) 0.020m/s, (b) 0.039m/s, (c) 0.079m/s. A rectangular with sharp corners is to be drawn. Grey line: experimental data. Green line: ideal trajectory. Red line: trajectory of 4-DoF simulation. Blue line: trajectory of full-DoF simulation. The starting point of each counter-clockwise loop is the left bottom corner.

The experimental data in **Fig. 3** consists of 20 loops of rectangular path following. However, we could not recognize fluctuation of the actual trajectory regardless of increasing the running speed. Note that the starting point of each loop remains the same. This is because sufficient time could be given for the system to release energy after each cycle. However, it is worth noting that such sufficient time delay may not be given practically. For example, it is not preferable for 3D printing when it could adversely affect the homogeneous extrusion of layers.

Furthermore, to obtain a numerical comparison between the simulation and experiment, contour error is defined as the smallest deviation from the desired contour to the actual position [18]. In the case of the rectangular path tasks, it is the distance between the ideal point of turning and the studied trajectory measured by an oblique line of 45° starting from the ideal point of turning. Mathematically, it can be expressed as

$$e = \sqrt{(x-x_0)^2+(y-y_0)^2}, |x-x_0| = |y-y_0| \qquad (17)$$

where e is the magnitude of error; (x, y) is a point on the studied trajectory; (x_0, y_0) is the corner point on ideal trajectory. For the experimental trajectory, the error is defined as the mean value of the error of each loop.

Magnitude of contour error with different running speed is plotted in **Fig. 4**. With the error in experiment acting as the baseline, the full-DoF model gave a good estimation of the linear trend of contour error. The 4-DoF model did predict a smaller contour error, particularly for the turning from the y- to the x-direction, as a result of the difference in their transient performances. Thus, the 4-DoF model showed a larger deviation from the experiment at high speed. Therefore, it can be concluded that the full-DoF model gives a better prediction of contour error at high speed.

We also found that the contour errors were linearly correlated to the running speed in both the simulations and the experiment. The discrepancies are shown by the dotted lines in **Fig. 4**. The discrepancies can be correlated with other practical factors, such as the nonlinear static friction, the pre-tension force of the belt, and the error of the tracking system (i.e., the first two types of error discussed in [19]), which show no clear dependence on the running speed.

B. Error analysis on system parameters

In addition, system parameters including mass, stiffness, and friction will also affect the magnitude of the contour error in terms of the transient response of the system. This influence is demonstrated by simulations with different parameters under the full-DoF model and an operation speed of 0.079m/s. The new parameters were attained by multiplying the parameters in **Table I** with a factor between 0.5 and 2 defined as relative parameters. Note that all masses were altered proportionally. The simulated maximum contour error with respect to relative mass, stiffness, and friction are shown in **Fig. 5**. Conclusions are summarized as follows.

- The magnitude of error shows little dependence on masses of pulleys and frames.
- The magnitude of error is proportional to the magnitude of friction and inversely proportional to the stiffness of belt.

These conclusions point out two significant ways to reduce the contour error by mechanical setup: 1) reducing friction and 2) increasing the stiffness of belt. Furthermore, they offer a pragmatic quantitative relation to estimate the magnitude of contour error under different mechanical setup prior to the experiment.

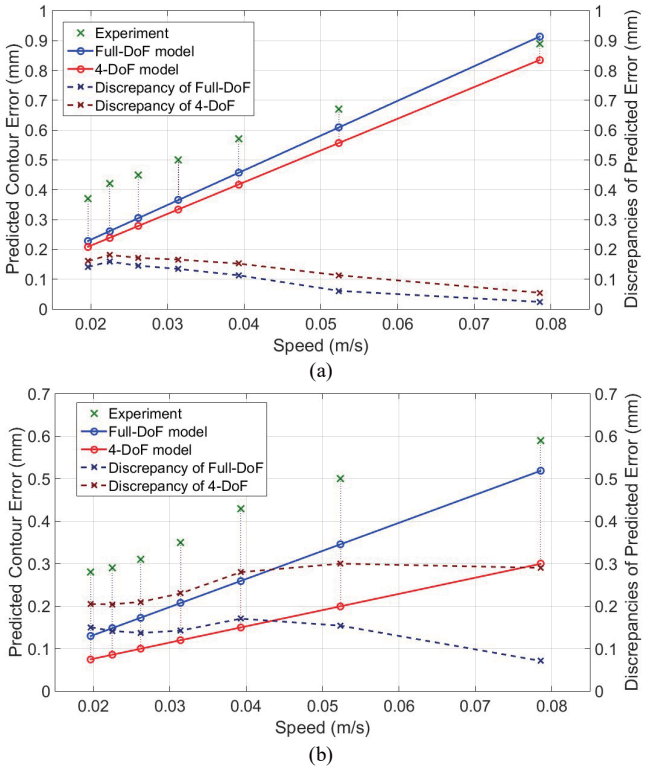

Fig. 4. The magnitude of contour error varied along the running speed during the right-angle turning from (a) *x*- to *y*-direction, (b) *y*- to *x*-direction. The dashed lines show the discrepancy between prediction and experiment.

IV. Conclusion

In this paper, dynamic modelling of a Cartesian motion system Core-XY is investigated. Core-XY has been widely utilized in many various applications, such as high-speed 3D printing, accredited to the low manufacturing cost of this system. Therefore, to identify the error due to the stiffness of belt, the system dynamics has been modeled. Experimental evaluation shows that the full-DoF dynamic model can attain an accurate estimation of contour error. A simplified modeling method has also been conducted, which has been proven to be effective only at low speed. A typical type of contour error for non-smooth contours at high-speed operation is highlighted based on the proposed dynamic model. In addition, its correlations with the running speed and system parameters were studied. In sum, a reliable approach to predict the accuracy of the Core-XY system is made possible through simulation. These simulations allow controllers to be tailored to reach a finer resolution of the end-effector.

Reference

[1] H. Lim, J.-W. Seo, and C.-H. Choi, "Position control of XY table in CNC machining center with non-rigid ballscrew," in *Proc. Amer. Control Conf.*, 2000, pp. 1542-1546.

[2] L. Abdullah, Z. Jamaludin, N. A. Rafan, J. Jamaludin, and T. H. Chiew, "Assessment on tracking error performance of Cascade P/PI, NPID and N-Cascade controller for precise positioning of xy table ballscrew drive system," in *2013 IOP Conf. Ser.: Mater. Sci. Eng.*, 2013, vol. 53, p. 012010.

[3] A. Hace, K. Jezernik, B. Curk, and M. Terbuc, "Robust motion control of XY table for laser cutting machine," in *Proc. of IECON '98*, 1998, vol. 2, pp. 1097-1102.

[4] B. Evans, *Practical 3D Printers: The Science and Art of 3D Printing*. New York: Springer, 2012.

[5] K. Itoh, M. Iwasaki, and N. Matsui, "Robust fast and precise positioning of ball screw-driven table system on machine stand," in *Proc. 8th IEEE Int. Workshop Adv. Motion Control*, 2004, pp. 511-515.

[6] S. C. K. Junoh *et al.*, "Evaluation of tracking performance of NPID double hyperbolic controller design for XY table ball-screw drive system," in *2017 11th Asian Control Conference (ASCC)*, 2017, pp. 665-670.

[7] W. Li and M. Rehani, "Modeling and control of a belt-drive positioning table," in *Proc. 22nd IEEE Int. Conf. Ind. Electron., Control, Instrum.*, Taipei, Taiwan, 1996, pp. 1984-1989.

[8] J.-P. Merlet, "Parallel manipulators: state of the art and perspectives," *Advanced Robotics,* vol. 8, no. 6, pp. 589-596, 1993.

[9] K. S. Sollmann, M. K. Jouaneh, and D. Lavender, "Dynamic modeling of a two-axis, parallel, H-frame-type XY positioning system," *IEEE/ASME Trans. Mechatronics,* vol. 15, no. 2, pp. 280-290, 2010.

[10] I. E. Moyer. (2012). *Implementation of CoreXY system*. Available: http://www.corexy.com

[11] W. Li and X. Cheng, "Adaptive high-precision control of positioning tables—Theory and experiments," *IEEE Trans. Control Syst. Technol.,* vol. 2, no. 3, pp. 265-270, 1994.

[12] Y. Hong and B. Yao, "A globally stable high-performance adaptive robust control algorithm with input saturation for precision motion control of linear motor drive systems," *Mechatronics, IEEE/ASME Transactions on,* vol. 12, no. 2, pp. 198-207, 2007.

[13] C.-I. Huang and L.-C. Fu, "Adaptive approach to motion controller of linear induction motor with friction compensation," *Mechatronics, IEEE/ASME Transactions on,* vol. 12, no. 4, pp. 480-490, 2007.

[14] S. Kulkarni and M. A. El-Sharkawi, "Intelligent precision position control of elastic drive systems," *IEEE Trans. Energy Convers.,* vol. 16, no. 1, pp. 26-31, 2001.

[15] A. Hace, K. Jezernik, and A. Sabanovic, "SMC with disturbance observer for a linear belt drive," *IEEE Trans. Ind. Electron.,* vol. 54, no. 6, pp. 3402-3412, 2007.

[16] A. Hace, K. Jezernik, and A. Sabanovic, "Improved design of VSS controller for a linear belt-driven servomechanism," *Mechatronics, IEEE/ASME Transactions on,* vol. 10, no. 4, pp. 385-390, 2005.

[17] T. Iwatsubo, K. Hasegawa, S. Arii, and K. Shiohata, "The formulation and dynamic analysis of a multiple belt system," *Journal of sound and vibration,* vol. 205, no. 3, pp. 293-307, 1997.

[18] J. Yang and Z. Li, "A novel contour error estimation for position loop-based cross-coupled control," *Mechatronics, IEEE/ASME Transactions on,* vol. 16, no. 4, pp. 643-655, 2011.

[19] Y. Koren and C. C. Lo, "Advanced controllers for feed drives," *Annals of the CIRP,* vol. 41, no. 2, pp. 689-698, 1992.